Conditioning Circuits for Nanoscale Perpendicular Spin Transfer Torque Magnetic Tunnel Junctions as Magnetic Sensors

Hugo Nicolas, Ricardo C. Sousa, Ariam Mora-Hernández, Ioan-Lucian Prejbeanu, Luc Hebrard, Jean-Baptiste Kammerer, Joris Pascal

Conditioning Circuits For Nanoscale Perpendicular Spin Transfer Torque Magnetic Tunnel Junctions As Magnetic Sensors

Hugo Nicolas, Ricardo C. Sousa, Ariam Mora-Hernández, Ioan-Lucian Prejbeanu, *Senior Member, IEEE*, Luc Hebrard, *Member, IEEE*, Jean-Baptiste Kammerer, and Joris Pascal

***Abstract*—This paper demonstrates a new type of magnetic sensor using a perpendicular spin transfer torque magnetic tunnel junction. The sensing element has a cylindrical shape of 50 nanometers in diameter and is to our knowledge among the smallest magnetic sensor ever reported. This paper describes the principle of operation of the sensing element and the associated signal processing electronics, which delivers a signal proportional to the external magnetic field. Experimental results are detailed and compared to state-of-the-art commercially available integrated magnetic sensors as well as published magnetoresistive sensors based on magnetic tunnel junctions with comparable size. The measured sensitivity of the developed sensor is 1.28 V/T, and its dynamic range reaches 80 mT. The measured noise level is 21.8 µT/√Hz. Two different operating principles of the proposed sensor are described and compared, one based on a time-to-digital converter and one based on a pulse-width-modulated signal. Both methods require only standard microelectronics components, which are suitable for a monolithic integration of the sensing element with its conditioning electronics. Subsequent improvements of the sensing element as well as conditioning electronics are required to further lower the noise level. The sensing element and its conditioning electronics are compatible with fabrication processes already used in magnetic random-access memory fabrication. This opens the way to mass production and addresses various markets such as consumer electronics, automotive, industrial sensing, physics experiments or medical devices.**

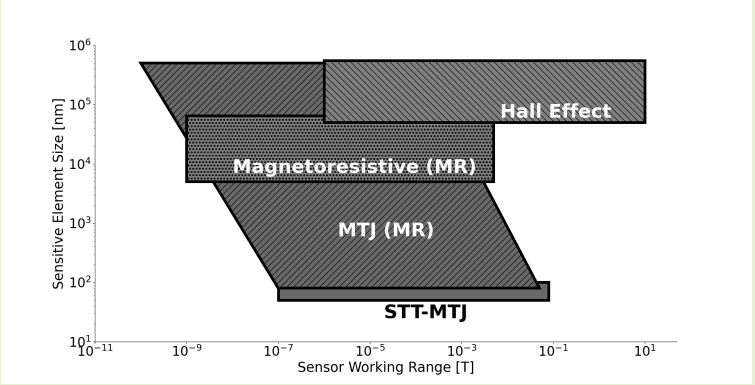

***Index Terms*—Magnetic sensor, magnetic tunnel junction, nanometer scale, spin transfer torque, STT-MRAM, STT-MTJ**

I. Introduction

MAGNETIC sensors are omnipresent in various applications such as consumer electronics, automotive, industrial sensing, physics experiments or medical devices. Thereby, many types of sensors are commercially available or currently being developed to extend the possibilities of new applications in a constantly growing market [1], [2].

Hall effect and magnetoresistive (MR) sensors are among the most popular magnetic sensors, used for their small size, low cost, and availability as integrated circuits (ICs). Hall sensors exhibit large measurement ranges and moderate noise performance whereas MR sensors exhibit low noise and moderate measurement ranges [3]. The sensitive element of both types of sensors typically covers a surface on the silicon die of about 100 µm^2 to 250,000 µm^2 [4]-[8]. The resulting magnetic field measurement corresponds to an average value of the magnetic field over the sensing element surface. In ICs, the sensing element is usually associated within the same die or chip with the conditioning and processing electronics required to output an accurate digital signal through standard communication bus, such as universal asynchronous receiver-transmitter (UART), inter-integrated circuit (I2C) or serial peripheral interface (SPI). Conditioning electronics includes for instance the biasing, or the noise and offset reduction circuitry while the signal processing includes the amplification, the filtering, or the analog-to-digital conversion.

Magnetoresistive sensors are based on a wide range of physical phenomena among which AMR (anisotropic MR),

Manuscript received XXXXXXX XX, XXXX; accepted XXXXXXX XX, XXXX. Date of publication XXXXXXXX XX, XXXX; date of current version XXXXXXX XX, XXXX. This work was funded by the Swiss Nanoscience Institute (No. A16.10) and by the ERC-2020-PoC (MAGALIGN No. 963895).

Hugo Nicolas and Joris Pascal are with the School of Life Sciences (HLS), University of Applied Sciences, 4132 Muttenz, Switzerland (e-mail: hugo.nicolas@fhnw.ch ; joris.pascal@fhnw.ch).

Luc Hebrard and Jean-Baptiste Kammerer are with the laboratory ICube, University of Strasbourg, 67000 Strasbourg, France (e-mail: luc.hebrard@unistra.fr ; jb.kammerer@unistra.fr).

Ricardo C. Sousa, Ariam Mora-Hernández and Ioan-Lucian Prejbeanu are with the laboratory Spintec, French Atomic Energy and Alternative Energies Commission (CEA), 38000 Grenoble, France (e-mail: ricardo.sousa@cea.fr ; ariam.mora-hernandez@cea.fr ; ioan-lucian.prejbeanu@cea.fr).

Digital Object Identifier XXXXXXXXXXXXXXXXXXXXXXXXXXXX

GMR (giant MR) or TMR (tunneling MR) with a massive increase of interest over the past decades [2]. Hence, magnetic tunnel junctions (MTJs) are nowadays frequently used as MR elements (i.e., TMR sensors) with different sizes, from tens of nm to hundreds of micrometers in various applications, mainly due to their high sensitivity and very low noise.

This paper presents a nanometric magnetic sensing element with two specific reading methods. The sensor is based on a cylindrical MTJ of 50 nm in diameter (0.0025 μm^2) and 1 to 2 nm in sense layer height. With these dimensions up to thousands of times smaller than standard MR and Hall sensors and similar to the smallest TMR sensors reported, we demonstrate a dynamic range of up to 80 mT, with a bandwidth of up to 30 kHz. A sensitivity of 1.28 mV/mT is achieved with a noise level of 21.8 $\mu T/\sqrt{Hz}$. The discrete conditioning and signal processing electronics are implemented with standard microelectronics components compatible with a future monolithic integration of the entire sensor system. In section II, the principles of MTJs are reminded. In section III, the MTJ samples and the experimental setup are presented. The principle of the sensor is then introduced in section IV. In section V, performance of the presented sensor are compared to state-of-the-art commercial sensors and published MR MTJs sensors. Finally, the experimental results and performance are discussed in sections VI and VII.

II. Magnetic Tunnel Junctions

Magnetic tunnel junctions are among recent and promising devices studied as an emerging memory technology for magnetic random-access memories, MRAMs, outperforming current technologies for low power embedded applications with some remaining technological challenges [9], [10].

These devices consist of a tunnel barrier of insulating non-magnetic material, usually MgO 1 to 2 nanometers thin, between two layers of ferromagnetic electrodes of similar thickness (Fig. 1). Because of the nanometric scale of the structure, different quantum phenomena can be observed in these devices such as quantum tunneling, tunnel magnetoresistance (TMR), as well as spin transfer torque (STT). As a result, the MTJ can simply be seen as a variable resistor with only two possible resistive states, either low resistance, parallel state (P), when the orientation of the two ferromagnetic layers are in the same direction or high resistance, antiparallel state (AP), when the orientation of the two ferromagnetic layers are in opposite directions.

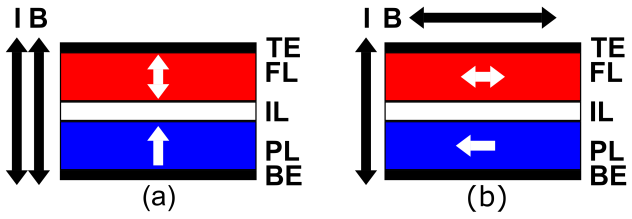

Fig. 1. Perpendicular MTJ (a) and in-plane MTJ (b). The direction of the switching current (I) and magnetic field (B) are indicated by the black arrows. The insulating layer (IL) is located between the free layer (FL) where the magnetization can be set in one of the two directions indicated by the white arrows. The pinned layer (PL) has its magnetization fixed in one direction (under normal condition), indicated by the white arrow. Two electrodes are used on the top (TE) and bottom (BE) to access the MTJ.

The state of the MTJ can be changed in two different ways, either by a strong enough magnetic field, or a strong enough current, through the STT effect. The switching between the two states follows a hysteresis loop, regardless the effect driving the reversal (Fig. 2), while the direction of the external magnetic field or current will define the state the MTJ will be set, either P or AP. Ideally, in the absence of stray field from the reference layer, the two switching currents, P to AP and AP to P, have the same absolute value and are only opposite in sign. Nevertheless, the absolute values of the two currents are usually slightly different, resulting in slightly shifted current hysteresis cycles.

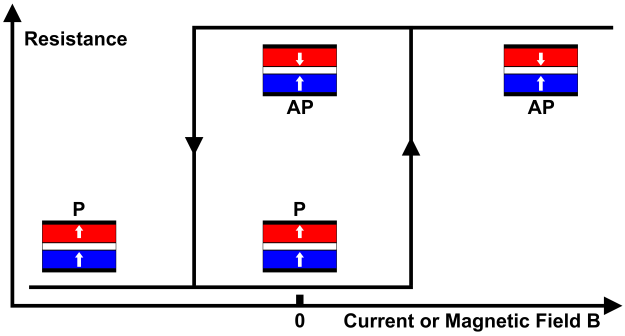

Fig. 2. Hysteresis cycle of a perpendicular MTJ, either induced by the current through the junction or the external magnetic field

Furthermore, the switching currents required to reverse the state of the junction are linearly related to the external magnetic field for the perpendicular magnetization configuration [11]. This creates a suitable situation for magnetic sensing as explained in the next sections. In both reversals, the switching of the junction is a stochastic process that depends exponentially on time and the ratio of retention energy barrier and thermal energy [12]. The center of the switching distribution, either when looking at the switching probability induced by current or magnetic field is called the critical switching value. For current induced switching, the critical values are therefore shifting linearly depending on the external magnetic field. While the junction is sensitive to the perpendicular (out-of-plane) external magnetic field, the in-plane field is unavoidable in real life applications. However, it has been demonstrated [11] that the effect of the in-plane field is negligible on the behavior of the junction.

III. Experimental MTJs and Setup

The junctions used are perpendicular magnetic anisotropy MTJs, or pMTJs, originally designed for MRAM, patterned to a vertical pillar (Fig. 3), with diameters ranging between 50 and 100 nanometers. The fabricated device complete stack is described in a separate published work [13].

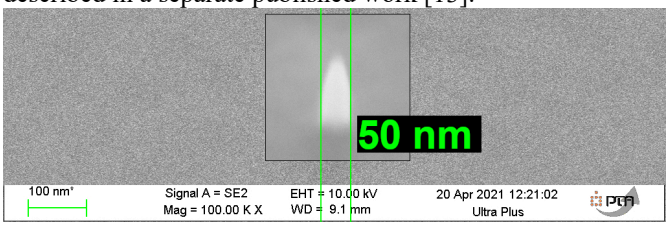

Fig. 3. SEM image of a 50-nm perpendicular MTJ (sensing unit)

The layer structure includes a Pt/Co multilayer based synthetic antiferromagnet (SAF) reference layer, coupled to a $FeCo_8B_{20}$ 1.2 nm bottom electrode. The tunnel barrier was

fabricated by natural oxidation of 0.8 nm Mg for 240 seconds. The top sense layer is comprised of an $FeCo_8B_{20}$ layer with a W 2/ Ta 1 nm capping layer. The wafer used in this work was annealed for 10 min at 350 °C. Higher annealing temperatures are expected to improve the measured TMR as can be concluded from our previous reported work [13]. Samples with W capping have been confirmed to withstand 400 °C annealing temperatures with a stack identical to the ones of the present wafer. This makes the junctions used compatible with standard back end of line (BEOL) process flows.

These MTJs demonstrate a TMR ratio between 60 % to 110 % (average of 91 %), calculated as the ratio of the resistance change, i.e., $(R_{AP} - R_P) / R_P$. The resistance of the devices is around 7 kΩ for the P state and 14 kΩ for the AP state with a coercive field of 40 mT (30-60 mT), i.e., hysteresis loop half-width. A typical loop offset of 14 mT (10-25 mT) corresponds to a loop shift favoring the P state. This results in sensitive elements tested with working ranges from -26 mT to 54 mT. The resistance-area product (RA) ranges between 12 to 40 Ω.μm² and the average thermal stability Δ is 41, defined by $\Delta = E_B/k_BT$, with E_B being the energy barrier.

One can note that the wafer used was originally fabricated with two wedges (i.e., thickness gradients) along the horizontal and vertical axis of the wafer on the MgO and $FeCo_8B_{20}$ free layer. Therefore, the reported parameters variations should not be considered as the result of standard fabrication variations. Performance of tested MTJs in the same regions showed very similar values. An in-depth statistical study using a wafer containing a single type of junction to analyze fabrication variability was considered premature at this proof-of-concept stage. In the following sections, the experiments and results described were carried over two similar MTJs with a nominal diameter of 50 nm.

The junctions are typically fabricated on a 4-inch (100 mm) diameter wafer, containing up to 20,000 devices. All the junctions on the wafer are connected by two square pads of approximately 200 μm x 200 μm, providing the electrical contact to the bottom and top electrodes of each MTJ (Fig. 4).

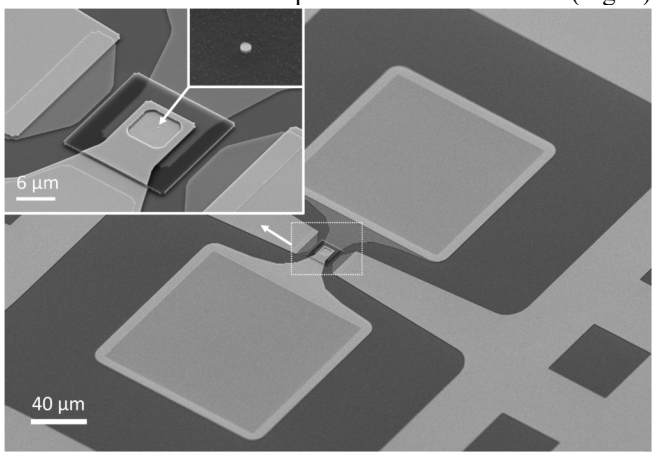

Fig. 4. SEM image of one device on the wafer. The two large pads are connected to the top and bottom electrode of the MTJ.

Our custom test setup consists of a Helmholtz coil with a diameter of 138 mm, arranged horizontally, capable of creating a magnetic field up to ± 8 mT along the vertical axis (Fig. 5). The Helmholtz coil is driven with a current amplifier, voltage-controlled by a waveform generator to create custom magnetic field waveforms. The wafer is placed in between the two coils such that the MTJ under test is always located in the region where the field is homogeneous. A custom non-magnetic SG (Signal-Ground) RF (radiofrequency) probe is used to access the pads and connects the MTJ to the electronics, currently implemented as a discrete version on a PCB (printed circuit board), using commercial electronic components (e.g., operational amplifiers, resistors, capacitors, etc.). The circuit is powered by an external standard power supply at ± 3.3 V.

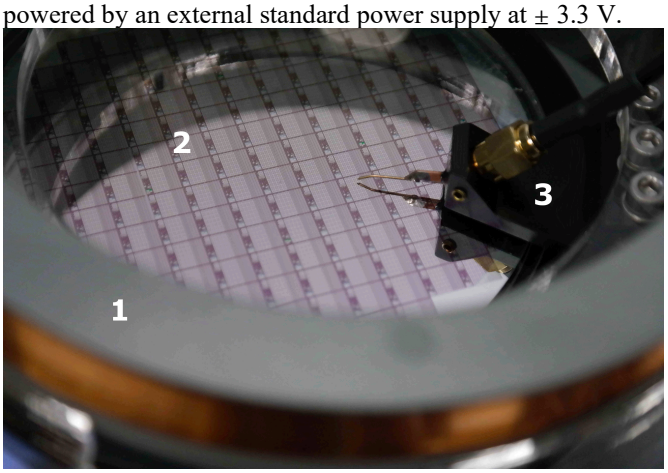

Fig. 5. Experimental setup (1. Helmholtz coil, 2. Wafer, 3. Probe). The sensing direction of the MTJs is perpendicular to the wafer.

IV. Sensor Principle and Performance

Using the key dependency between the switching currents and the external magnetic field, the sensor operating principle is to track the evolution of the switching currents in time and relating it to the variation of the external magnetic field. To facilitate the acquisition of signals, voltage instead of current control is used, and the switching voltages are tracked instead.

To achieve this, an ac voltage is applied across the junction. We decided to use a sine wave to avoid higher harmonics in the signal, although other waveforms could also be used such as triangular or exponential rise/fall waveforms. When the voltage across the junction reaches a critical value, it induces a switching event, a reversal from AP to P state (APP) or P to AP state (PAP). The resistance of the junction drops for APP reversal and increases for PAP. Following Ohms' law, this creates a current discontinuity (Fig. 6). The reversal process is typically only a few nanoseconds long [14], [15].

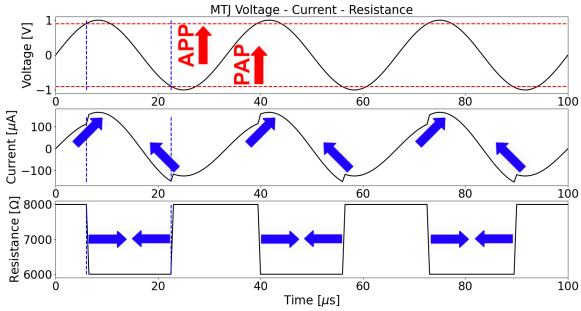

Fig. 6. Sensor working principle (simulation). When the input voltage across the MTJ reaches the critical APP (positive voltages) or PAP (negative voltages) values, shown by the red thresholds, the resistance is changing suddenly, resulting in discontinuities in the current passing through the MTJ. The arrows indicate how the signals are changing for an increasing external magnetic field.

By measuring the current through the MTJ using a differential amplifier and a shunt resistor, and by passing the resulting signal in a second order high-pass filter (HPF) with high enough cutoff frequency to remove the low frequency harmonics, one can determine the switching times, by detecting spikes at the output of the HPF (Fig. 7 and Fig. 8). In our case, an active high-pass filter using a Sallen-Key configuration with a cutoff frequency of 725 kHz is used. These spikes can then be converted into a standard digital signal (i.e., 0 or 1) using a comparator with a tuned threshold.

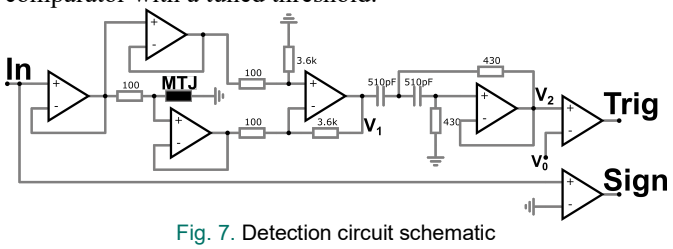

Fig. 7. Detection circuit schematic

In Fig. 7, the ac input signal (In) is applied to a first buffer, then through the shunt resistor of 100 Ω in series with the MTJ. The voltage across the shunt is measured using a differential amplifier (V_1) and filtered through the high-pass filter (Fig. 8). The resulting signal (V_2) is then passed through a comparator with a 60-mV threshold (V_0), outputting pulses (Trig) with standard logical levels. A second comparator is used to sample the sign of the input signal in respect to the ground (Sign), allowing the events to be classified either as APP or PAP events. The value of the shunt of 100 Ω, relatively high, is used to limit the output current of the input buffer within its specified absolute maximum output current. This large current could be reached if the MTJ is shorted, which can happen for junctions breaking down when applying voltages above the breakdown limit, typically ± 1.5 V for the investigated junctions.

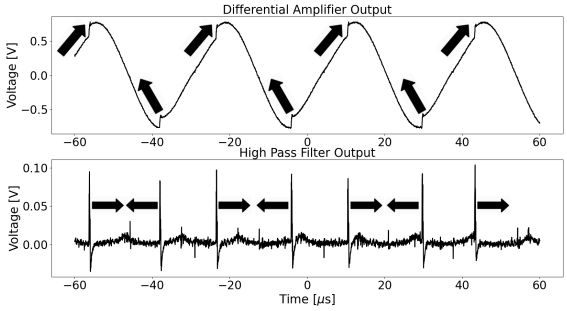

Fig. 8. Measured output of differential amplifier (V_1) showing regular APP and PAP reversals and HPF output (V_2), creating 100 mV and 250 ns pulses. One can see the asymmetrical time differences between APP-PAP and PAP-APP reversals as a result of asymmetrical APP and PAP switching voltages of the junction. The arrows indicate how the signals are changing for an increasing external magnetic field.

When a switching event is detected, the voltage applied on the junction is sampled and saved. By performing a high-enough number of measurements and averaging the results, one can obtain the value of the critical voltages and calculate the magnetic field. However, this method has two drawbacks. As a large number of samples is required to average precisely the voltages, it is necessary to have at least tens to hundreds of events to obtain a single magnetic field measurement, increasing the storage area requirement. Furthermore, a fast and high-resolution analog-to-digital converter (ADC) is also required to sample the voltage values. This performance level requires expensive and complex ADCs. These drawbacks can be overcome with two alternative methods presented in the following sections A and B.

In both methods, a sine wave signal from a waveform generator with a peak-to-peak amplitude of 2 V and a frequency of 30 kHz is applied across the MTJ. Hence, one can obtain reversals and switching pulses occurring roughly at 60 kHz, i.e., two reversals per period. The frequency has been arbitrarily chosen while the amplitude corresponds to the STT switching voltages of these MTJs, around ± 1 V respectively for APP and PAP events. To avoid introducing phase noise, the stability of the signal applied is between 30 to 50 ppm, compatible with most commercial IC oscillators and relatively easy to design. However, the pulses will not happen exactly at 60 kHz because of the intrinsic switching stochasticity and the external magnetic field. In this case, if the external magnetic field increases, the APP and PAP critical voltages change, APP voltages becoming more positive, while the PAP voltages become less negative. As a result, the time between APP and PAP pulses will shorten while the time between PAP and APP will increase. The magnetic field is therefore directly related to the time between each APP-PAP and PAP-APP reversal events.

A. Time-to-Digital Converter (TDC)

To measure these time differences, a 96 MHz, 16-bits timer (i.e., counter) from an STM32F411 microcontroller (MCU) is used. Each detected pulse triggers an interrupt on the MCU. The value of the timer as well as the sign of the input sine wave, used to distinguish the nature of the event, are saved in the microcontroller's internal memory. Using a custom Python script, we then reconstruct the time variations between APP and PAP, as well as between PAP and APP switching events.

Using the described TDC method, we observed a sensitivity for both APP-PAP and PAP-APP events respectively of 91.0 and -94.4 ns/mT (8.74 and -9.06 LSB/mT) (Fig. 9). The signals are symmetrical and opposite in sign, and exhibit a resolution, defined by the 96 MHz timer of 10.42 ns/LSB (~112 μT/LSB). Despite using a non-linear input signal, the integral nonlinearity error (INL) is measured respectively at 1.42 and 1.18 % of the full scale (FS). The asymmetry in the switching currents is responsible for this small asymmetry in the switching times.

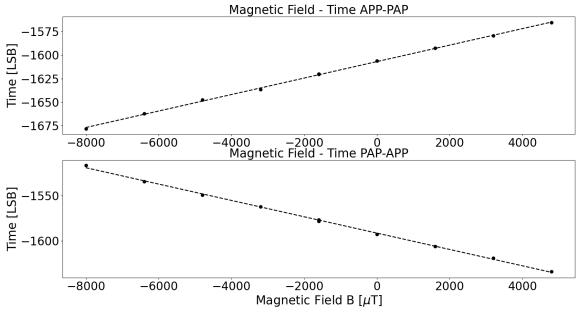

Fig. 9. Measured output sensitivity for both APP-PAP and PAP-APP events (each point is averaged from 400 samples)

When performing a measurement of an external magnetic field sine wave at 20 Hz with an amplitude ranging between -8 to +8 mT, one can measure output values oscillating according to a sine wave at the correct amplitude (~16 mT) for both events, and a measured frequency of ~18.6 Hz for both events.

This frequency difference, centered around 20 Hz and randomly distributed when repeating the measurements, is induced by the switching probability noise as well as the reduced number of measured periods. However, the measurements of longer periods of time converges toward 20 Hz. Other sources of noise, such as phase noise from the waveform generator, are negligible compared to the noise induced by the stochasticity. By performing a moving median over 300 samples (10 ms), the output can be smoothed at the expense of the sensor bandwidth, reduced to 100 Hz (Fig. 10). A moving median is used instead of a moving average to minimize the impact of statistically unsignificant data points induced by the stochasticity.

Because of the non-linear sine wave signal applied across the junction, a larger dispersion can be seen at the extremums of the sine wave. Using a linear signal, such as a triangular waveform, reduces this dispersion. Thanks to the 30 kHz input signal frequency, this method allows the measurement of ac signals up to 15 kHz (Nyquist frequency). In practice, the maximum frequency would be lower because of the large number of points required to properly average the voltages. However, by using both APP-PAP and PAP-APP events combined through interpolation, this maximum frequency could be doubled up to 30 kHz even if the resulting signal would still exhibit a large white noise.

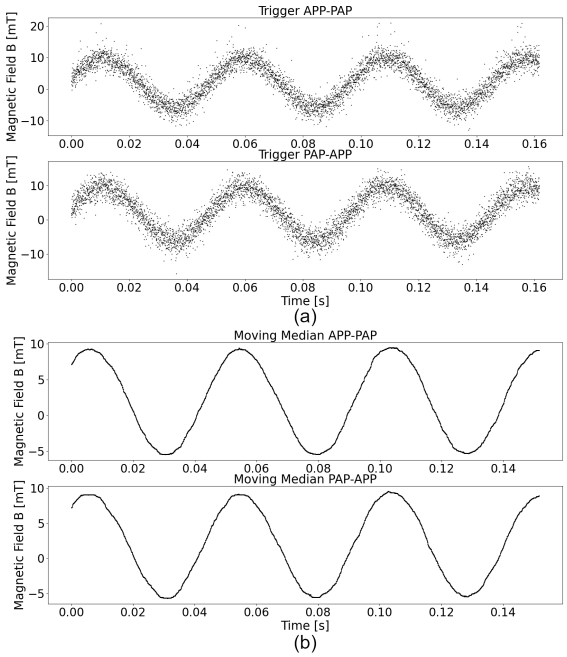

Fig. 10. Measurement of a 20 Hz, ± 8 mT sine wave external magnetic field. APP-PAP time and PAP-APP time are showing large noise induced by switching probability (a). Moving median over 300 measurement points (10 ms) for both signals (b).

In the absence of applied external magnetic field, excepted the surrounding background magnetic field, the output signals exhibit a noise described by a Gaussian distribution, with a peak-to-peak amplitude for APP-PAP and PAP-APP events of respectively 275 and 240 LSB (2.86 and 2.50 µs) and a standard deviation σ respectively of 36.2 and 34.2 LSB (377 and 356 ns). The calculated root mean square (RMS) noise at the output of the sensor is respectively 41.6 and 36.3 LSB (~4.3 mT). Surprisingly, the analysis of the noise spectral density of the sensor shows no 1/f noise. The reasons for this absence will be discussed in section V. The measured averaged noise spectral density for both events is respectively 3.07 and 2.94 ns/√Hz for APP-PAP and PAP-APP events. This corresponds to an equivalent noise of 32.4 µT/√Hz (Fig. 11).

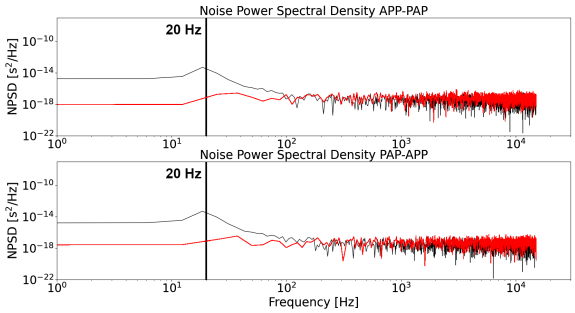

Fig. 11. Measured noise power spectral density (NPSD) with (black) and without (red) the 20 Hz external magnetic field

Assuming that T is the period and A is the amplitude peak of the input signal, R_{AP}, R_P, R_S are respectively the AP, P and shunt resistance values and S_{APP}, S_{PAP} are the intrinsic sensitivity of the MTJ, then the sensitivity of the sensor using the TDC method can be described by (1) and (2) as long as the input sine wave is approximated as a linear signal.

$$\frac{dT_{APP\rightarrow PAP}}{dB} = \frac{-T}{4.A}.\left[\frac{S_{APP}.(R_S+R_{AP})}{R_{AP}} + \frac{S_{PAP}.(R_S+R_P)}{R_P}\right] \quad (1)$$

$$\frac{dT_{PAP\rightarrow APP}}{dB} = \frac{T}{4.A}.\left[\frac{S_{PAP}.(R_S+R_P)}{R_P} + \frac{S_{APP}.(R_S+R_{AP})}{R_{AP}}\right] \quad (2)$$

With the presented STT-MTJs, the intrinsic absolute sensitivity is on average 4.41 mV/mT for both APP and PAP events. This gives an expected average sensitivity of ± 74 ns/mT, which is in agreement with the experimental data considering that the use of a sine wave (non-linear) increases this time-domain sensitivity. The intrinsic sensitivity of pMTJs is described in [11] for MTJs switched with short pulses of tens of ns and depends on the intrinsic Gilbert damping parameter as well as being inversely proportional to the STT in-plane efficiency pre-factor. However, one can note that STT-MTJs operated with continuous voltage sweep are slightly different than pulsed-operated STT-MTJs, and (1) and (2) are not taking into account all the dynamic effects of the reversal processes.

B. Pulse-Width-Modulation (PWM)

Alternatively, a second reading approach can be used. This second method uses a clocked set-reset (SR) flip-flop circuit. The clock input is connected to the switching pulses output (Trig) of the detection circuit, while the set and reset are respectively connected to the sign (Sign) and inverted sign (nSign) outputs (Fig. 12).

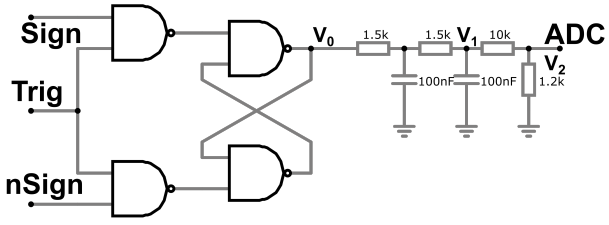

Fig. 12. PWM converter circuit schematic

As a result, one can construct a pulse-width-modulated (PWM) signal (Fig. 13) [16]. The duty cycle of such signal changes according to the external magnetic field. The resulting

PWM signal (V_0) is then passed through a simple second order passive low-pass filter (LPF) with a cutoff frequency much lower than the 30 kHz input signal, in this case 1050 Hz, implemented as two simple RC (resistor-capacitor) filters. The output signal (V_1) is an analog voltage whose average value is proportional to the applied magnetic field. Finally, a simple voltage divider using two resistors with a ratio of 10:1.2 (i.e., 8.3:1) is used to scale the voltage (V_1) down to a compatible range for the ADC (V_2), in this case limited to +256 mV. The scaled signal (V_2) is then directly sampled by the ADC, in this case a 16-bits sigma-delta ADC, offering a resolution of 7.8125 µV/LSB with an output data rate of 128 Hz.

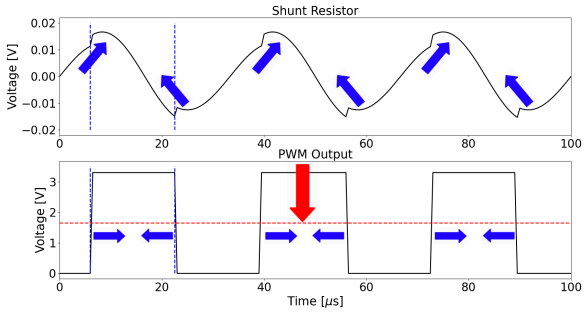

Fig. 13. Voltage across shunt resistor and PWM output (simulation). The LPF filters the PWM signal (V_0), resulting in a dc signal as shown by the red signal (V_1). The arrows indicate how the signals are changing for an increasing external magnetic field.

The results obtained using this second approach also showed a working principle, with a sensitivity of around -164 LSB/mT (-1.28 mV/mT) (Fig. 14). Despite using a non-linear input signal, the integral nonlinearity error is measured at 1.79 % FS.

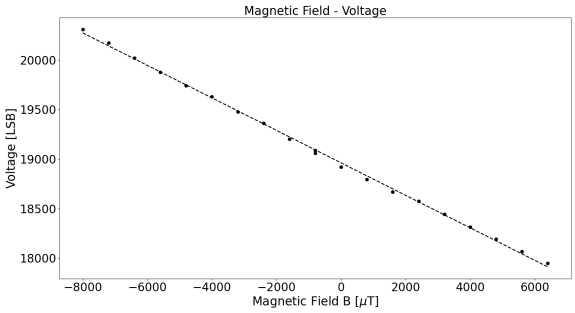

Fig. 14. Measured output sensitivity (each point is averaged from 400 samples)

When performing a measurement of an external magnetic field sine wave of 300 mHz ranging between -8 to +8 mT, one can measure output values properly oscillating and following a sine wave at the correct amplitude (~16 mT) and frequency (~340 mHz). The 40 mHz difference is induced by the uncalibrated time between ADC samples. One can note that this difference is constant when repeating measurements and could be corrected by carefully measuring the exact time between ADC samples but was not considered necessary so far for the demonstration of the sensor working principle. Significantly less dispersion is visible as the switching probability noise is partially filtered by the LPF. A larger dispersion is still visible at the extremums of the sine waveform, caused by the non-linear signal (sine wave) used across the junction (Fig. 15).

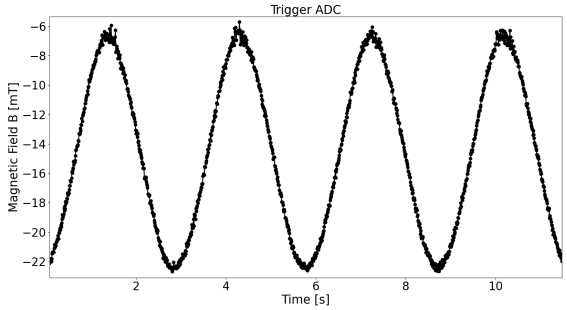

Fig. 15. Measurement of a 300 mHz, ± 8 mT sine wave external magnetic field. The offset is induced by the inaccurate voltage divider.

Noise analysis was performed in the same conditions as described for the previous method. In the absence of external magnetic field, the output values exhibit a noise with a Gaussian distribution, with a peak-to-peak amplitude of 262 LSB (2 mV) and a standard deviation σ of 33.3 LSB (260.1 µV). The calculated RMS noise at the output of the sensor is 39.6 LSB (~309 µT). Despite filtering large parts of the switching probability noise, the remaining noise is still mostly induced by the stochasticity of the MTJ. The noise spectral density shows a low 1/f noise with a corner frequency of 1 Hz and white noise. The measured averaged white noise spectral density is approximately 28 µV/√Hz, corresponding to an equivalent noise of 21.8 µT/√Hz (Fig. 16).

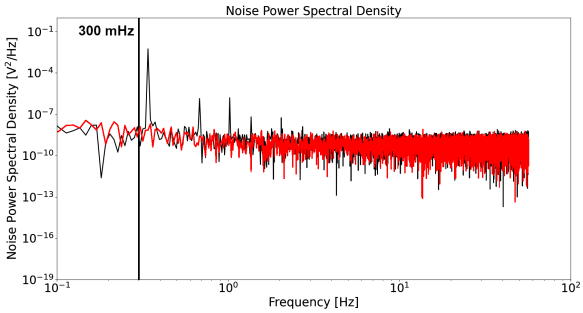

Fig. 16. Measured noise power spectral density (NPSD) with (black) and without (red) the 300 mHz external magnetic field

Using (1) and (2), describing the sensitivity of the sensor using the TDC method, one can establish the output sensitivity of the sensor using the PWM method. Assuming that the frequency of the PWM signal is high enough (arbitrarily defined) compared to the LPF cutoff frequency, the average value V_{PWM} of the PWM signal with a low level V_L of 0 V and high level V_H of 3.3 V is given by (3).

$$\frac{dV_{PWM}}{dB} = \frac{V_H}{T} \cdot \left[\frac{dT_{APP \rightarrow PAP}}{dB}\right] \quad (3)$$

This gives on average -7.3 mV/mT, scaled down by a factor of 8.3 introduced by the voltage divider, which gives an average sensitivity of -0.88 mV/mT. This is in agreement with the obtained experimental value, considering that the use of a sine wave (non-linear) increases the time-domain sensitivity and therefore directly influences the voltage sensitivity.

V. Performance

Table I and II compare the obtained results with four high-performance commercial integrated monolithic magnetic sensors, with performance extracted from their datasheets. All these sensors are standard surface mounted devices (SMD) and

output data directly in a binary format as for the described STT-MTJ sensor (Table I), or analog format (Table II). These sensors were chosen to illustrate the diversity of available high-performance commercial devices. One can note the Memsic MMC5603NJ, a high-resolution AMR sensor with a package reported to be the smallest on the market (0.43 mm^3). The NVE SM324-10E is a single axis MTJ-based sensor based on MR principle, showing a higher sensitivity and lower range, despite probably using a much larger micron-size MTJ with a size of tens to hundreds of square micrometers in order to reduce the noise [17]-[24]. For analog sensors (Table II), as all the signal processing electronics is not included on the chip (e.g., ADC), the size of the sensing element can be increased resulting in higher performance. One can note that all the reported MR sensors are using a Wheatstone bridge configuration to achieve the highest sensitivity and lowest noise.

Table III compares our obtained results with published experimental results of MgO-MTJs exhibiting comparable diameters and implemented as MR sensors. MTJs with micron-size diameters were also included for reference. These sensors are based on a standard MR principle and thus require a relatively simple signal processing scheme with slightly less components than the presented STT-MTJ solution. Typically, such MR sensors require at least a low-noise amplifier with a low-pass filter before being sampled by an ADC. However, the standard ADC architectures available to achieve µV resolution (e.g., Sigma-Delta or Successive Approximation Register, SAR) typically require thousands of transistors, making the difference between our reading circuits and MR MTJs reading circuits negligible. Comparatively, the TDC method, only possible with the presented sensor specific reading principle, makes a significant difference since the total number of transistors is greatly reduced with the removal of the ADC.

As reported in published work [24], MR MTJs suffer from five main types of noises, all independents, which are thermal electronic and magnetic noises, shot noise, 1/f noise and random telegraph noise (RTN). In addition, the reading electronics adds another layer of noise, which can be negligible in some situations (e.g., low frequency operating ranges and/or small diameters MTJs). At small diameters, the main sources of noise typically considered are thermal magnetic noise and 1/f noise. While the thermal magnetic noise is reported to be independent from the frequency, the 1/f noise is increasing inversely proportional to the frequency and both noises increase with the reduction of the diameter of the junction. Therefore, the noise of MTJs is greatly increasing at low frequencies and for smaller diameters. For this reason, most of the reported and commercial MR MTJs are in the µm or even in the mm range. For instance, in [20], 120 nm circular MR MTJs showed a 1/f noise with a corner frequency higher than 100 kHz and a NPSD of 2 µT/√Hz at 1 kHz. Hence, the 50 nm MTJs used in this work could easily exhibit a corner frequency in the MHz range, that could explain the absence of any visible 1/f corner frequency up to the frequency of 10 kHz measured with the TDC method.

Different methods have been reported in [24] to reduce these noises but all involve the addition of complexity to the sensor such as flux concentrators, Wheatstone bridge configuration or chopping stabilization circuits, as in many Hall sensors. These

TABLE I

PERFORMANCE OF 4 HIGH-PERFORMANCE DIGITAL COMMERCIAL SENSORS AND THE PRESENTED STT-MTJ SENSOR

	AKM AK09970N (3 axis)	Metrolab MagVector™ MV2 (3 axis) – Z axis	Memsic MMC5603NJ (3 axis)	NVE SM324-10E (1 axis)	STT-MTJ (1 axis) – TDC	STT-MTJ (1 axis) – PWM
Technology	Hall	Hall	MR (AMR)	MR (MTJ)	STT-MTJ	STT-MTJ
Range	± 36 mT	± 100 mT	± 3 mT	± 2 mT	> ± 8 mT (80 mT)	> ± 8 mT (80 mT)
Data rate	1262 Hz	375 Hz	75 Hz	300 Hz	30 kHz	128 Hz
Resolution	1 LSB = 1.1 µT	1 LSB = 3.4 µT	1 LSB = 6.25 nT	1 LSB = 238 pT	1 LSB = 112 µT	1 LSB = 6 µT
Noise (RMS)	5 µT = 4.5 LSB	3.7 µT = 1.1 LSB	150 nT = 24 LSB	*2.2 µT = 9483 LSB*[b]	4.3 mT = 38.95 LSB	309 µT = 39.6 LSB
Sensitivity	909 LSB/mT	289 LSB/mT	163 840 LSB/mT	4 194 304 LSB/mT	8.9 LSB/mT	164 LSB/mT
Size[a]	*10 µm x 10 µm to 500 µm x 500 µm*	200 µm x 200 µm	*10 µm x 10 µm to 100 µm x 100 µm*	*1 µm x 1 µm to 50 µm x 50 µm*	50 nm x 50 nm	50 nm x 50 nm

[a]The size indicated is the size of the sensitive element. When the size is not given in the datasheet, the typical range of the technology is given instead
[b]Experimental measurement

TABLE II

PERFORMANCE OF 4 HIGH-PERFORMANCE ANALOG COMMERCIAL SENSORS AND THE PRESENTED STT-MTJ SENSOR

	Multi Dimension AMR2501 (1 axis)	Metrolab MagVector™ MV2 (3 axis) – Z axis	Honeywell HMC1001 (1 axis)	Multi Dimension TMR2901 (1 axis)	STT-MTJ (1 axis) – TDC	STT-MTJ (1 axis) – PWM
Technology	MR (AMR)	Hall	MR (AMR)	MR (MTJ)	STT-MTJ	STT-MTJ
Range	± 200 µT	± 100 mT	± 200 µT	± 2 mT	> ± 8 mT (80 mT)	> ± 8 mT (80 mT)
NPSD	160 pT/√Hz (1 Hz)	225 nT/√Hz	181 pT/√Hz (1 Hz)	2 nT/√Hz (1 Hz)	32.4 µT/√Hz	21.8 µT/√Hz
Linearity	1.2 % FS	7.7 % FS (0.16 % FS)	1 % FS	0.3 % FS	1.3 % FS	1. 79 % FS
Sensitivity	125 mV/mT (5 V)	17.71 mV/mT (3.3 V)	160 mV/mT (5 V)	250 mV/mT (1 V)	92.7 ns/mT	1.28 mV/mT
Size	3 mm x 3 mm	200 µm x 200 µm	NA	1 mm x 1.2 mm	50 nm x 50 nm	50 nm x 50 nm

TABLE III

PERFORMANCE OF 6 PUBLISHED MR MTJ SENSORS AND THE PRESENTED STT-MTJ SENSOR

	[18] (1 axis)[a]	[19] (1 axis)[a]	[20] (1 axis)[a]	[21] (1 axis)[a]	[22] (1 axis)[a]	[23] (1 axis)[a]	STT-MTJ (1 axis) – TDC[b]	STT-MTJ (1 axis) – PWM[b]
Technology	MR (MTJ)	MR (MTJ)	MR (MTJ)	MR (MTJ)	MR (MTJ)	MR (MTJ)	STT-MTJ	STT-MTJ
Range	± 14 mT	± 30 mT	± 14 mT	± 1 mT	± 1.5 mT	± 50 mT	> ± 8 mT (80 mT)	> ± 8 mT (80 mT)
NPSD (10 Hz)	NA	NA	18 µT/√Hz	NA	4.5 nT/√Hz	NA	32.4 µT/√Hz	21.8 µT/√Hz
Linearity	NA	< 1 % FS	NA	NA	NA	NA	1.3 % FS	1.79 % FS
Sensitivity	0.5 %/mT	0.2 %/mT	2 %/mT	9.1 %/mT	39 %/mT (170 mV/V/mT)	1 %/mT	92.7 ns/mT	1.28 mV/mT
Size	120 nm x 120 nm	80 nm x 80 nm	120 nm x 120 nm	3 µm x 6 µm	5 µm x 60 µm	400 nm x 100 nm	50 nm x 50 nm	50 nm x 50 nm

[a]In-plane MgO-MTJ
[b]Out-of-plane MgO-MTJ

modifications directly increase the total area of the sensing element. Using larger MTJs also remains an efficient solution to enhance performance and lower the noise.

However, the presented sensing principle of the STT-MTJ is not based on MR principle. Therefore, another important source of noise, the stochasticity of the MTJ, should be considered. This noise source has already been presented in section II. For any given voltage and magnetic field applied, the MTJ has a corresponding probability of switching from one state to another. Using the presented MTJs, the measured ΔV, i.e., voltage range over which APP or PAP reversal events are observed for a given magnetic field, is approximately 50 mV. This creates a pure white noise in our measurements, corresponding to a pure magnetic white noise of approximately 11 mT peak-to-peak. This pure white noise is covering any other smaller noise. However, by calculating the NPSD in the TDC method using the moving median data of the noise measurements, we observe a continuous and linear (log-log) decrease of the noise for an increasing frequency, which corresponds to 1/f noise. Therefore, in the TDC method, no 1/f noise can be measured due to the large white noise. The low frequency 1/f noise observed in the PWM method is in reality induced by the electronic components and not the MTJ itself.

We conclude that the large noise observed in our measurements is mainly induced by the stochasticity of the MTJ. An in-depth analysis of such probabilistic noise could possibly lead to stack optimization and lower noise. Nevertheless, averaging larger samples remains the best option so far to achieve lower noise with the presented reading methods. Similarly to the intrinsic sensitivity analysis, different models and equations describe the stochasticity of STT-MTJs operated with short pulses [12], [25]-[27]. However, no models nor equations were found for continuous voltage sweep and in-depth studies would also be required to adapt, confirm, or establish new equations.

VI. Outlook

This magnetic sensor architecture shows a working principle demonstrated with two possible measurement methods, each presenting their own advantages and drawbacks. The TDC method allows fast measurements with few components required (e.g., binary counter), creating a device with high sampling speed, compact layout design and comparatively low resolution. In contrast, the PWM method offers performance with higher resolution, lower bandwidth, while requiring a larger layout induced by the ADC and the large capacitors of the LPF. In addition, the PWM method presents no issue in terms of memory requirements or resolution as for the TDC. Hence, the advantage of the TDC method is that it does not require any fast, high-resolution ADC, which is replaced by a simple binary counter, more suitable for monolithic integration. However, a large memory is still required to save data points. For instance, one second of measurement requires 1.02 Mb of memory, equivalent to 127.5 kB. Another limitation of the TDC approach is its resolution, which is directly related to the maximum frequency of the counter. Therefore, to increase the resolution, either a faster counter or a more advanced time-to-digital converter is required. With the presented TDC, an equivalent voltage resolution of approximately 1.25 mV/LSB (~112 µT/LSB) is obtained. Hence, to obtain an equivalent resolution in the range of few microvolts for one count, which can be achieved with standard ADCs, a counting frequency of tens of GHz would be required. This is extremely difficult and complex to handle. On the other hand, reducing the frequency of the input signal would also increase the equivalent resolution, by reducing the slope of the voltage, reducing at the same time the sampling rate of the sensor. For instance, to get an equivalent resolution of 10.42 µV/LSB (~1.1 µT/LSB), the frequency of the input signal must be slowed down to 250 Hz for a 96 MHz timer.

However, in both methods implemented so far, high-performance commercial products still present noise and resolution better than our measured performance as a result of the much larger sensing elements. On the other hand, published MR MTJs with comparable dimensions exhibit similar performance with a stack optimized for sensing applications.

Hence, to improve performance, the use of a linear signal (e.g., triangular signal) or a faster input frequency are among possible changes. One can note that the TDC method would require the introduction of more complex time-to-digital techniques in order to increase the resolution and the use of build-in averaging digital circuit to reduce the memory requirements. Sensing-oriented MTJs with higher field sensitivity and lower stochasticity are also among required further improvements to lower the noise. MTJs with diameters as small as 20 nm are also in development and shall be evaluated in future works for sensing applications in particularly to evaluate their stochasticity.

To conclude about the main advantages of the presented STT-MTJ sensor, it includes a very small sensitive element of tens of nanometers with an extremely small area (0.0025 µm²). The compact conditioning electronics required is also an advantage, requiring only a few operational amplifiers and passive components. In contrast to other types of MR sensors (e.g., AMR or microelectromechanical systems, MEMS), MTJs benefit from the absence of destructive field, and can withstand large field ranges without being permanently damaged, whereas such MR sensors can be irreversibility damaged within tens to hundreds of millitesla. In addition, the demonstrated nanometric sensor also benefits from room temperature operating range. In comparison, high-sensitivity nanometric sensors such as nano-SQUIDs (Superconducting Quantum Interference Devices) work only at very low temperature (typically few Kelvin) and require complex circuits to be operated [28]-[30], hence targeting completely different applications. Finally, while the Hall sensors can be natively fabricated using standard complementary metal-oxide semiconductor (CMOS) technologies, MR sensors, including MR MTJs (in-plane), usually require specific or non-standard technologies. However, the presented STT-MTJ sensor uses perpendicular MTJs. Therefore, as STT-MRAMs are almost exclusively being developed using out-of-plane MTJs to avoid the high-density and low-power-consumption issues that arise in in-plane MTJs at small diameters [31], [32], the presented STT-MTJ sensor is likely to be fully compatible with CMOS technology for monolithic integration and mass production. The development of emerging memories, including STT-MRAMs, greatly increased over the past years with an expected $36 billion market in 2030 [10]. Hence, with the strong industrial

interest and development of STT-MRAMs, such STT-MTJs sensors could even be natively supported by foundries.

The demonstrated STT-MTJ sensor could find applications in diverse domains from industrial applications to the medical field, embedded either in a single small chip, or as an array of sensing units. Among application examples, one can list industrial applications such as current sensing, fault detection, or system alignment, such as photolithographic masks, to medical applications with near-field sensing, magnetic tracking systems, or magnetic camera with extremely high density.

VII. Conclusion

This paper has presented a specific reading architecture for nanometric magnetic sensors using perpendicular spin transfer torque magnetic tunnel junctions. The proposed architecture was successfully tested through two different methods and experimental measurements. Despite initial performance described which are still below state-of-the-art commercial products performance in terms of noise, the measured noise is close to the reported noise for the state-of-the-art MR MTJs with comparable sizes and sensing-oriented stacks. Hence, the design of dedicated junctions specifically targeting field sensing applications as well as improved electronics will allow us to enhance the performance of the presented sensor, intrinsically suitable for monolithic integration.

References

[1] M. A. Khan, J. Sun, B. Li, A. Przybysz, and J. Kosel, "Magnetic sensors-a review and recent technologies", *Engineering Research Express*, vol. 3, no. 2, June, 2021, 10.1088/2631-8695/ac0838.

[2] C. Zheng et al., "Magnetoresistive Sensor Development Roadmap (Non-Recording Applications)", *IEEE Transactions on Magnetics*, vol. 55, no. 4, pp. 1-30, April, 2019, 10.1109/TMAG.2019.2896036.

[3] P. Ripka, *Magnetic Sensors and Magnetometers*, Artech House, 2000.

[4] S. Yamada, R. Haraszczuk, M. Kakikawa, and H. Hoang. (2012). "Micron size GMR magnetic sensor with needle structure". AIP Conference Proceedings, 10.1063/1.4716331.

[5] L. Caruso, "Giant magnetoresistance based sensors for local magnetic detection of neuronal currents", Ph.D. dissertation, Université Pierre et Marie Curie, Paris, France, 2015.

[6] W. Wang, Y. Wang, L. Tu, Y. Feng, T. Klein, and J.-P. Wang, "Magnetoresistive performance and comparison of supermagnetic nanoparticles on giant magnetoresistive sensor-based detection system", *Scientific Report*, vol. 4, July, 2014, 10.1038/srep05716.

[7] J. Lee, Y. Oh, S. Oh, and H. Chae, "Low Power CMOS-Based Hall Sensor with Simple Structure Using Double-Sampling Delta-Sigma ADC", *Sensors,* vol. 20, no. 18, September, 2020, 10.3390/s20185285.

[8] K. Vervaeke, E. Simoen, G. Borghs, and V. Moshchalkov, "Size dependence of microscopic Hall sensor detection limits", *The Review of scientific instruments*, vol. 80, 2009, 10.1063/1.3160105.

[9] E. Liu, "Materials and designs of magnetic tunnel junctions with perpendicular magnetic anisotropy for high-density memory applications", Ph.D. dissertation, KU Leuven University, Leuven, Belgium, 2018.

[10] J. Choe. (2021). "Memory Technology 2021: Trends & Challenges". International Conference on Simulation of Semiconductor Processes and Devices (SISPAD), pp. 111-115, 10.1109/SISPAD54002.2021.9592547.

[11] A. A. Timopheev, R. Sousa, M. Chshiev, L. D. Buda-Prejbeanu, and B. Dieny, "Respective influence of in-plane and out-of-plane spin-transfer torques in magnetization switching of perpendicular magnetic tunnel junctions", *Physical review B*, vol. 92, September, 2015, 10.1103/PhysRevB.92.104430.

[12] L. Tillie, E. Nowak, R. C. Sousa, M. C. Cyrille, B. Delaet, T. Magis, A. Persico, J. Langer, B. Ocker, I.-L. Prejbeanu, and L. Perniola. (2016). "Data retention extraction methodology for perpendicular stt-mram". IEEE International Electron Devices Meeting (IEDM), 10.1109/IEDM.2016.7838492.

[13] J. Chatterjee, E. Gautier, M. Veillerot, R. C. Sousa, S. Auffret, and B. Dieny, "Physicochemical origin of improvement of magnetic and transport properties of STT-MRAM cells using tungsten on FeCoB storage layer", *Applied Physics Letters*, vol. 114, 2019, 10.1063/1.5081912.

[14] R. Tomasello, V. Puliafito, B. Azzerboni, and G. Finocchio, "Switching Properties in Magnetic Tunnel Junctions With Interfacial Perpendicular Anisotropy: Micromagnetic Study", *IEEE Transactions on Magnetics*, vol. 50, July, 2014, 10.1109/TMAG.2014.2307280.

[15] N. Maciel, E. Marques, L. Naviner, Y. Zhou, and H. Cai, "Magnetic Tunnel Junction Applications", *Sensors*, vol. 20, 2020, 10.3390/s20010121.

[16] J.-B. Kammerer, L. Hebrard, M. Hehn, F. Braun, P. Alnot, and A. Schuhl, "A Two-Axis Magnetometer Using a Single Magnetic Tunnel Junction", *IEEE Sensors Journal*, vol. 4, pp. 313-321, 2004, 10.1109/JSEN.2004.824232.

[17] P. P. Freitas, R. Ferreira, S. Cardoso, and F. Cardoso, "Magnetoresistive sensors", *Journal of Physics: condensed matter*, vol. 19, no. 16, 2007, 10.1088/0953-8984/19/16/165221.

[18] D. C. Leitao, A. V. Silva, R. Ferreira, E. Paz, F. L. Deepack, S. Cardoso, and P. P. Freitas, "Linear nanometric tunnel junction sensors with exchange pinned sensing layer", *Journal of Applied Physics,* vol. 115, 2014, 10.1063/1.4869163.

[19] Z. M. Zeng, P. Khalili Amiri, J. A. Katine, J. Langer, K. L. Wang, and H. W. Jiang, "Nanoscale magnetic tunnel junction sensors with perpendicular anisotropy sensing layer", *Applied Physics Letters,* vol. 101, 2012, 10.1063/1.4744914.

[20] D. Leitao, P. Elvira, A. Silva, A. Moskaltsova, S. Knudde, L. Francis, R. Ferreira, S. Cardoso, and P. Freitas, "Nanoscale Magnetic Tunnel Junction Sensing Devices With Soft Pinned Sensing Layer and Low Aspect Ratio", *IEEE Transactions on Magnetics,* vol. 50, 2014, 10.1109/TMAG.2014.2320606.

[21] Weifeng Shen, Benaiah D. Schrag, Matthew J. Carter, Jin Xie, Chenjie Xu, Shouheng Sun, and Gang Xiao, "Detection of DNA labeled with magnetic nanoparticles using MgO-based magnetic tunnel junction sensors", *Journal of Applied Physics,* vol. 103, 2008, 10.1063/1.2832880.

[22] L. Huang, Z. H. Yuan, B. S. Tao, C. H. Wan, P. Guo, Q. T. Zhang, L. Yin, J. F. Feng, T. Nakano, H. Naganuma, H. F. Liu, Y. Yan, and X. F. Han, "Noise suppression and sensitivity manipulation of magnetic tunnel junction sensors with soft

magnetic Co70.5Fe4.5Si15B10 layer", *Journal of Applied Physics,* vol. 122, 2017, 10.1063/1.4990478.
[23] C. Albon, A. Weddemann, A. Auge, K. Rott, and A. Hütten, "Tunneling magnetoresistance sensors for high resolutive particle detection", *Applied Physics Letters,* vol. 95, 2009, 10.1063/1.3179241.
[24] Z. Q. Lei, G. J. Li, W. F. Egelhoff, P. T. Lai, and P. W. T. Pong, "Review of Noise Sources in Magnetic Tunnel Junction Sensors", *IEEE Transactions on Magnetics*, vol. 47, no. 3, pp. 602-612, March, 2011, 10.1109/TMAG.2010.2100814.
[25] A. Nisar, S. Dhull, S. Mittal, and B. K. Kaushik, "SOT and STT-Based 4-Bit MRAM Cell for High-Density Memory Applications", *IEEE Transactions on Electron Devices*, vol. 68, no. 9, pp. 4384-4390, 2021, 10.1109/TED.2021.3097294.
[26] A. F. Vincent et al., "Spin-Transfer Torque Magnetic Memory as a Stochastic Memristive Synapse for Neuromorphic Systems", *IEEE Transactions on Biomedical Circuits and Systems*, vol. 9, no. 2, pp. 166-174, April, 2015, 10.1109/TBCAS.2015.2414423.
[27] M. Wang, and Y. Jiang, "Compact model of nanometer STT-MTJ device with scale effect", *AIP Advances,* vol. 11, 2021, 10.1063/9.0000049.
[28] Y. Shibata, S. Nomura, H. Kashiwaya, S. Kashiwaya, R. Ishiguro, and H. Takayanagi, "Imaging of current density distributions with a Nb weak-link scanning nano-SQUID microscope", *Scientific Reports*, 2015, 10.1038/srep15097.
[29] M. Schmelz, Y. Matsui, R. Stolz, V. Zakosarenko, T. Schönau, S. Anders, S. Linzen, H. Itozaki, and H.-G. Meyer, "Investigation of all niobium nano-SQUIDs based on sub-micrometer cross-type Josephson junctions", *Superconductor Science and Technology,* 2015, 10.1088/0953-2048/28/1/015004.
[30] J. C. Gallop, "SQUIDs: some limits to measurement", *Superconductor Science and Technology,* 2003, 10.1088/0953-2048/16/12/055.
[31] D. Apalkov, B. Dieny, and J. M. Slaughter, "Magnetoresistive Random Access Memory", *Proceedings of the IEEE*, vol. 104, no. 10, pp. 1796-1830, October, 2016, 10.1109/JPROC.2016.2590142.
[32] J. G. Webster, S. Peng, Y. Zhang, M. Wang, Y. Zhang, and W. Zhao, "Magnetic Tunnel Junctions for Spintronics: Principles and Applications" in Wiley Encyclopedia of Electrical and Electronics Engineering, J. G. Webster, Ed., 2014, 10.1002/047134608X.W8231.

Hugo Nicolas received the B.S. degree in electronics and M.S. degree in microelectronics from the University of Strasbourg, France in 2019 and 2021 respectively. He is currently pursuing the Ph.D. degree at the University of Strasbourg, France, and the University of Applied Sciences, Muttenz, Switzerland since September 2021. His research focuses on the development of a new generation of magnetic sensors using spin transfer torque magnetic tunnel junctions.

Ricardo Sousa received his M.S. degree in Engineering Physics in 1995 from the University of Lisbon and Ph.D. degree in Applied Physics from the Instituto Superior Técnico in Lisbon, for his work on MRAM based on spin dependent magnetic tunnel junctions. He has been working on Magnetic Tunnel Junctions and MRAM at Spintec since 2002, leading the MRAM group there since 2007. He is co-author of 3 book chapters, more than 130 articles, and 16 patents. His research interests are in the field of Spintronic applications, developing sensors and MRAM concepts based perpendicular magnetic anisotropy written by spin transfer torque and all optical switching methods. For his research in thermally assisted MRAM switching, he was a European Descartes Prize finalist in 2006.

Ariam Mora-Hernández received the B.S. degree in physics from University of Veracruz, Mexico in 2012, M.S. degree in theoretical physics from the Center for Research and Advanced Studies of the National Polytechnic Institute, Mexico in 2015 and Ph.D. in Experimental physics at Durham University, United Kingdom in 2020. Since 2021, he is a postdoctoral researcher at the Spintec (CEA), France. His research focuses on nanomagnetism, material physics, interfacial phenomena in thin-films and fabrication of MTJs for sensor applications.

Lucian Prejbeanu holds a Ph.D. in Physics from University of Strasbourg (2001). Senior Member IEEE, he is the executive director of Spintec research laboratory in Grenoble. He is an expert in the field of nanomagnetism and spintronics for magnetic memories and sensors. After his Ph.D., Dr. Prejbeanu joined Spintec, where he namely pioneered scientific work on thermally assisted MRAM. Based on this proof-of-principle awarded by the European Descartes Prize for Research in 2006. Dr. Prejbeanu participated in the creation of the start-up company Crocus Technology. As R&D Director of Crocus, Dr. Prejbeanu led the technological transfer and received in 2012 the joint SEE-IEEE Brillouin prize. Dr. Prejbeanu has authored more than 100 scientific publications and book chapters and is inventor of 46 patents. He is coordinator of the memory pillar of Spintronic Factory, a European network founded in 2016, co-director of the Upstream Technological Platform PTA, one of main nanofabrication centers of RENATECH, French academic network of nanofabrication technology centers and member of the Advisory Committee of IEEE Magnetics.

Luc Hebrard received in 1990 the Engineer and master's degrees in Microelectronics from Ecole Centrale de Lyon (France), and the Ph.D. degree in Microelectronics from ECL in 1993. He held a post-doctoral position at the CNM in Barcelona (Spain) from 1994 to 1995 and was appointed Associate Professor at the University of Strasbourg (Unistra, France) in 1995. From 2004 to 2005, he was a visiting researcher in the Electronic Instrumentation Laboratory at the Technical University of Delft (The Netherlands). He received in 2005 the Accreditation for Research Supervision degree from Unistra and was appointed Full professor at Unistra in 2006. He is with the ICube laboratory and works in the field of integrated instrumentation and its applications, as well as in the field of sensors modeling, and development of specific CAD tools for the design of integrated systems. He was the coordinator of 3 research projects funded by the French Agency of Research (ANR), and scientific head in ten other research projects from ANR or industry. He is co-author of 110 papers in international conferences and journals. He is a member of the IEEE society. He is involved in several program committees of international conferences and is a member of the steering committee of IEEE NEWCAS.

Jean-Baptiste Kammerer received the Ph.D. degree in microelectronics from the University Louis Pasteur, Strasbourg, France, in 2004. He is currently with the ICube Laboratory, University of Strasbourg, as an Associate Professor. His research interests include integrated sensors, low-noise circuits design, systems and devices' modeling, and heterogeneous systems' design.

Joris Pascal received in 2005 the Engineer and master's degrees in electrical engineering from Ecole Centrale Supélec (France), and the Ph.D. degree in Microelectronics from the University of Strasbourg (France), in 2008. He held scientist and senior scientist positions at ABB Switzerland, Corporate research in Baden-Dättwil (Switzerland) from 2009 to 2015 and was appointed Full Professor at the University of Applied Sciences and Arts Northwestern Switzerland, School of Life Sciences (Switzerland) in 2015. He is with the Institute of Medical Engineering and Medical Informatics and leads the Sensors and Electronics laboratory. He works in the field of instrumentation and its applications in biomedical engineering. He has developed the first Vertical Hall Device in standard CMOS technology, as well as several self-calibrated current and voltage sensors. He was scientific head in eight other research projects from SNF, SNI, Innosuisse or industry. He is co-author of 51 papers in international conferences and journals and the inventor of eight patents. He is a member of the Swiss Nanoscience Institute (SNI).